

**CORRECTION OF ULTRASONIC ARRAY IMAGES TO IMPROVE  
REFLECTOR SIZING AND LOCATION IN INHOMOGENEOUS  
MATERIALS USING A RAY-TRACING MODEL**

G.D. Connolly, M.J.S. Lowe, J.A.G. Temple

*UK Research in NDE*

*Imperial College London*

*SW7 2AZ*

*UK*

S.I. Rokhlin

*Edison Joining Technology Center*

*The Ohio State University*

*1248 Arthur E. Adams Drive*

*Columbus*

*OH 43221*

Original submission: 14 July 2009

Revised submission: 31 October 2009

## **Abstract**

The use of ultrasonic arrays has increased dramatically within recent years due to their ability to perform multiple types of inspection and to produce images of the structure through post-processing of received signals. Phased arrays offer many advantages over conventional transducers in the inspection of materials that are inhomogeneous with spatially varying anisotropic properties. In this paper, the arrays are focused upon austenitic steel welds as a representative inhomogeneous material. The method of ray-tracing through a previously developed model of an inhomogeneous weld is shown, with particular emphasis on the difficulties presented by material inhomogeneity. The delay laws for the structure are computed and are used to perform synthetic focusing at the post-processing stage of signal data acquired by the array. It is demonstrated for a simulated austenitic weld that by taking material inhomogeneity and anisotropy into account, superior reflector location (and hence superior sizing) results when compared to cases where these are ignored. The image is thus said to have been corrected. Typical images are produced from both analytical data in the frequency-domain and data from finite element simulations in the time-domain in a variety of wave modes, including cases with mode conversion and reflections.

PACS number(s): 43.20.Jr, 43.35.Cg

Keywords: Inhomogeneous, Ray-tracing, Ultrasonics, Weld Inspection

## I. INTRODUCTION

In recent years, the use of ultrasonic arrays has increased dramatically due to their flexibility, rapidity and ease of inspection when compared to single element transducers. Rapid increases in both computing power and storage capacities, and corresponding decreases in cost have paved the way for the development of improved modelling capabilities and imaging algorithms, with notable contributions from<sup>1-3</sup>.

Some researchers have applied the superior imaging performance of the ultrasonic array to generate images of internal reflectors<sup>4</sup>, the reflectors of interest being defects. However, limitations have been noted (see, for instance<sup>5</sup>) when the methods are applied to inhomogeneous materials due to the phenomenon of ray path deviation, making effective focusing of the array and hence the sizing and location of defects unreliable in images. In this paper, means of correcting these images are presented, applicable to any inhomogeneous and anisotropic material provided a model exists that accounts for the spatial variation in material properties to allow the computation of delay laws. Although this approach is of broad applicability, it is demonstrated here in the specific context of the non-destructive testing and inspection of austenitic steel welds.

Within the petro-chemical and nuclear industries, austenitic steels are favoured for use in engineering applications, particularly for the fabrication of piping and pressure vessels. They are used for their excellent resistance to corrosion and oxidation<sup>6</sup>, and have demonstrated high strength and toughness as compared to typical carbon steels<sup>7</sup>, and have the advantage that post-welding heat treatment need not be applied due to the high resistance to brittle fracture. These components may typically be subjected to cyclic and heavy loading, and as such, any crack-like defects that may have been formed during the welding process may propagate during service. In industry, regular monitoring of joints and other critical components takes place to evaluate the location, size and shape of internal defects<sup>5</sup>.

In addition to ultrasonics, commonly used techniques for weld inspection include radiography, a method that tends to be favoured due to the wealth of experience and technical expertise available<sup>8</sup>. Until recently, the capabilities of ultrasonic inspection of austenitic stainless steels were limited due to scattering and beam-steering<sup>9</sup>, phenomena that do not affect radiographic inspection. However, radiography represents a high associated cost of both inspection and downtime for the plant and for this reason, amongst others, a reliable method of ultrasonic inspection of austenitic steel is sought.

Studies of micrographs of welds have revealed that the grains tend to develop curved and elongated shapes in the direction of maximum heat flow, resulting in the formation of an anisotropic inhomogeneous material<sup>11</sup>. Beads that are the result of separate passes are generally visible. Partial melting of the previous passes by the current pass gives rise to epitaxial growth of grains between neighbouring beads. The grains are of the order of a centimetre in length, and since the inspection frequencies are typically 2-5 MHz, the wavelength is comparable to or smaller than the grain dimension. Rays are thus fully exposed to the material anisotropy and follow a curved path as dictated by the orientation of the elastic constants of the material. This phenomenon is known as beam-steering and many studies have sought to fully understand its causes<sup>12-14</sup>. The other phenomenon of scattering is not dealt with in this paper, where it is assumed that the two phenomena are separable, but further information can be found in the literature, for instance<sup>15</sup>.

Yet further difficulty is introduced by the fact that it is difficult to generalise the microstructure of the weld, being a function of the metallurgical composition of the parent metal and the weld metal, the welding temperature and the physical orientation of the weld during the welding process. If one were to assume the austenitic weld to be isotropic and homogeneous when performing inspections, errors in defect location would be likely to occur. To combat this, the literature has proposed weld models<sup>16</sup>, through which rays are

traced in order to improve understanding of wave behaviour within, for instance, austenitic steel V-welds. A concise introduction to this problem is found in Halmshaw<sup>17</sup>.

Using a similar approach based on a simplified weld model originally proposed by Ogilvy<sup>18</sup>, this paper demonstrates the computation of delay laws for a simulated austenitic steel weld in 2D, presents a graphical qualitative treatment of ray properties and then shows examples of their use on signal data collected from full finite element (FE) simulations.

## II. THEORY

In this section, the relevant aspects of elastic wave behaviour are reviewed in order to set out the terminology and the underlying fundamentals for the rest of this paper. Readers interested in replicating the ray-tracing model described later would find this section useful. Those wishing to find a fuller treatment may consult, for example, chapter 2 of Harker<sup>19</sup>.

In an unbounded elastic solid, the propagation of waves causes particles of the medium to become displaced from their resting positions linearly in a cyclical fashion. The phase of the wave is a property that describes where along the displacement cycle is a particular point of this medium. Lines that join points of constant phase describe wavefronts, and the velocity along which these wavefronts propagate is known as the phase velocity  $c$ .

### A. Bulk wave behaviour

The idea of a group velocity may have first been proposed by Russel<sup>20</sup>, who spoke of the velocity of a group of waves as distinct from the velocity ‘of the individual waves of which it is composed’. Though his work was extended by Stokes, it was Lord Rayleigh who eventually specified a relationship<sup>21</sup> between the group velocity  $V$ , the wavenumber  $k$ , and the angular frequency  $\omega$  in material waves:

$$V = \frac{d\omega}{dk}. \quad (1)$$

By means of substitution, the following relations were also derived:

$$c = \frac{\omega}{k}; \quad V = c + k \frac{dc}{dk}. \quad (2)$$

Propagating elastic waves in isotropic elastic solids are classed as either longitudinal or transverse. In a longitudinal wave, the particles are given a displacement parallel to the direction of propagation of the phase velocity and in a transverse wave the particles are displaced perpendicularly. These are the only types of propagating waves within an unbounded body. Surface waves are not dealt with in this paper. A third type of wave that is relevant to the wave calculations above the first critical angle is the evanescent wave, which may be generated at an interface (as seen in Sec. II. B). In the case of the evanescent wave, the particles of the medium move periodically and elliptically rather than linearly. In this case, the polarisation vector becomes complex, where the imaginary components represent the phase shift between the motions along the principle axes of the vector.

In this paper, it is assumed that the velocities of bulk waves do not vary with frequency. Experiments show for such welds that this assumption is reasonable for frequencies below 5MHz (for instance, see chapter 7 of<sup>22</sup>). Phase and group velocities in the isotropic material are equivalent though in generally anisotropic media, these velocities are neither necessarily the same nor act in the same direction, and the polarisation vector does not, as is the case in isotropic media, lie either parallel or perpendicular to the phase vector.

Here a method of determining wave properties given only the phase vector is summarised. From this point henceforth the implied index summation convention applies for subscripted  $i$ ,

$j$ ,  $k$  and  $l$ . The following general wave propagation equation relates the stress  $\sigma$  to the displacement vector  $\mathbf{u}$ , the density  $\rho$  and spatial position  $\mathbf{x}$ :

$$\frac{\partial \sigma_{ik}}{\partial x_k} = \rho \ddot{u}_i. \quad (3)$$

Hooke's law relates the stresses to the displacements in terms of a matrix of elastic constants  $\mathbf{C}$

$$C_{ijkl} \frac{\partial^2 u_k}{\partial x_l \partial x_j} = \rho \ddot{u}_i. \quad (4)$$

A general solution to (4) in tensor form is

$$u_k = A p_k \exp(i(k_j x_j - \omega t)). \quad (5)$$

with  $\mathbf{p}$  as the unit polarisation vector and  $\mathbf{k}$  as the vector of the wavenumber. The double derivative of (5) is substituted into the left hand side of (4) to yield

$$C_{ijkl} k_j k_k = \rho \omega^2 \delta_{il}. \quad (6)$$

Here,  $\delta_{ij}$  takes a value of one if  $i = j$  and a value of zero when  $i \neq j$ . The number of homogeneous equations, roots and velocities are all equal to the number of spatial dimensions in the system. Given also that  $c^2 = \omega^2/k^2$ , one may simplify (6) thus:

$$|\Gamma_{il} - \rho c^2 \delta_{il}| = 0 \quad (7)$$

where  $\Gamma = C_{ijkl} n_j n_k$ , and is called the Green-Christoffel acoustic tensor with  $\mathbf{n}$  being a vector describing the direction cosines of the wavevector. The numbers of homogeneous equations, roots and velocities are equal to the number of spatial dimensions in the system, and if the eigensystem method is applied to (7), it is found that the (vector of) eigenvalues  $\lambda$  and the (matrix of) eigenvectors  $\mathbf{v}$  are

$$\lambda_a = \frac{\rho}{m_a^2} \text{ and } v_a = p_a \quad (8)$$

respectively with  $1 \leq a \leq 3$ , and with the phase slowness  $\mathbf{m} = \mathbf{k}/\omega$ . The group velocity  $\mathbf{V}$  is related to the phase slowness by

$$V_a = \frac{1}{\rho} C_{ajkl} p_j p_k m_l. \quad (9)$$

## B. Wave behaviour at an interface

The prediction of properties of waves reflected and refracted from an interface is fundamental to the study of elastic wave propagation. In this paper a review is presented pertaining only to cases involving well-bonded interfaces between solids.

In three dimensional space, three waves are reflected and three are transmitted. In this paper, the approach used by Rokhlin et al.<sup>23</sup> is followed, where a sextic equation is constructed whose solutions yield the component of the phase slownesses normal to the interface. The other two components are already known, since all phase velocities (and hence phase slownesses) are in a single plane perpendicular to the interface. Complex conjugate

pairs produced from this equation indicate the presence of evanescent waves, whose properties are summarised in Table I. Once the phase slownesses are known, the methods described in Sec. II. A are used to compute the polarisation vector and the phase and group velocities.

At this point, the remaining unknown quantities are the wave amplitudes and phases. To find these, boundary conditions are enforced to ensure continuity of displacement and stress. The components of displacement along all three principal axes, the direct stress normal to the boundary and the two components of shear stress that have a component normal to the boundary must sum to zero. These boundary conditions concerning the six waves are rearranged to form a matrix of the said size. If it is assumed that there is only one incident wave striking the interface, one may write

$$A^I p_j^I + \sum_{a=1}^6 A^a p_j^a = 0 \quad (10)$$

and

$$\frac{A^I C_{13jk} p_j^I k_k^I}{c^I} + \sum_{a=1}^6 \frac{A^a C_{13jk} p_j^a k_k^a}{c^a} = 0 \quad (11)$$

where superscript  $\beta$  is the wave index and superscript  $I$  indicates a property of the incoming wave, the interface is the 12 plane and all waves are in the 13 plane. The components of (10) and (11) pertaining to the incident wave are placed on the other side of the equation, since the properties are known. The unknown values  $A$  are taken from the matrix to form a vector  $\xi$ , such that

$$\mathbf{q} = \mathbf{Q}\xi \quad (12)$$

where  $\mathbf{Q}$  represents the terms in the right hand sides of (10) and (11), and  $\mathbf{q}$  the terms on the left hand side. The matrix is inverted and the problem is solved for  $\xi$ . From this, the reflection and transmission coefficients are determined from the moduli and the changes in phase are determined from the arguments. The energy  $U$  of the wave varies cyclically with the displacement, but only the mean value normal to the interface is important, and may be calculated from the following formula from Lancelleur et al.<sup>24</sup>:

$$U_3 = \frac{|A|^2 \omega C_{3jkl} m_l (p_j^* p_k k_l + p_j p_k^* k_l^*)}{4} \quad (13)$$

If evanescent waves are present, the solution of (12) yields complex values of amplitude. Due to the complex phase slownesses, (13) reveals that evanescent waves transmit no energy but only store it. The 3-component of the resultant phase velocity is entirely imaginary, meaning that the cyclical particle motion amplitude decays exponentially as one moves away from the interface.

### III. WELD MODEL

Most butt welds do not change along the welding pass. Therefore the model used here assumes that material properties of a weld cross section do not change with respect to distance along the weld. The grains within the weld cross section are bent due to the way they have solidified during welding. This is the reasoning behind the introduction of the continuously inhomogeneous material.

The exact nature of the weld is unknown. The imaging results in this paper have been derived using a simplified 2D representation of the austenitic weld to mimic the general variation in material properties where the grain structure is ignored. The weldment takes the form of a continuously inhomogeneous V-section between two homogeneous parent metal regions, separated by two straight weld boundaries as illustrated in Fig. 1. In the weld region, the orientation  $\theta$  of the crystal z-axis relative to the global y-axis is given by the expression from Ogilvy<sup>18</sup>

$$\tan \theta = \begin{cases} -\frac{T(D+z \tan \alpha)}{x^n}, & x \geq 0 \\ \frac{T(D+z \tan \alpha)}{(-x)^n}, & x < 0 \end{cases} \quad (14)$$

where  $x$  and  $y$  are coordinates in a system whose origin is at the bottom of the weld centreline,  $T$  and  $n$  are parameters associated with the formation of the orientation structure,  $D$  is the distance from the centreline to the bottom corner of the weld, and  $\alpha$  the angle that the boundary between the weld and the surrounding material makes with the centreline. Each of the four weld parameters may take a different value for either side of the weld. The orientations produced from this formula take the form illustrated in Fig. 1. This paper adopts a transversely isotropic weld material used previously by Roberts<sup>25</sup> and whose elastic constants are listed in Table II. All anisotropy is confined to the operating plane, and hence the group and phase velocities lie in the same plane due to material symmetry. The isotropic steel is assigned the properties listed in Table III.

To propagate a ray, it is given a starting position (generally within the homogeneous region) and a phase vector. The following procedure is applied to the ray-tracing system within the weld model:

- (i) The methods outlined in Sec. II. A. are used to find its group vector and group velocity that determine its travel course and speed.
- (ii) The ray is allowed to propagate until it encounters an interface, a guaranteed occurrence due to the enclosed environment.
- (iii) If the ray has reached the backwall, it is arrested and treated as an incident wave upon a single interface as described in Sec. II. B., and the appropriate choice of reflected ray completes the evolution process. If a reflected ray of the required mode is not available (the typical reason would be that the critical angle for that mode has been exceeded), the ray terminates.
- (iv) If the ray has reached the upper surface or the sides of the model, it is also terminated.
- (v) If the ray has reached the weld boundary, then the methods of Sec. II. B. are used but in this case it is a transmitted ray that is sought. If a transmitted ray of the required mode is not available, the ray is terminated.
- (vi) When the ray is travelling within an inhomogeneous material, a boundary (let us apply the term 'non-physical' to these boundaries) must be applied after each time step to account for the continuous variation in material properties. The boundary is perpendicular to the gradient of  $\theta$  at the ray's position after each step, and the ray is treated as though it had crossed through this boundary. The material properties at the incident side of the boundary pertain to those of the ray's position at the previous step, and the properties on the other side to the ray's current position.

The ray path is thus determined by a succession of nonphysical and physical boundaries. Simulations have been carried out using the finite element (FE) software package ABAQUS<sup>26</sup> to validate the predictions of reflected and transmitted ray properties due to interaction at a single boundary. The verification methods have been described in<sup>27</sup>. Close agreement of the

ray properties with the theory has been observed across a variety of cases, including at a boundary between two anisotropic materials of the same elastic constants but different orientation.

#### IV. DELAY LAW COMPUTATION

To compute the delay laws, which are used to construct and correct the image, one employs Fermat's principle, which applies to any wave propagation, electromagnetic or elastic. In a general medium with spatially varying elastic constants, the time of travel for a ray between A and B is given by

$$D' = \int_A^B \frac{ds}{V(r)}. \quad (15)$$

Fermat's principle is that signals travel along a path with a travel time  $D'$  that has a stationary value with respect to variations in the path A-B<sup>28</sup> (usually a minimum, although in principle a maximum is possible). A trial-and-error approach is used for the computation, similar to that proposed in Sec. 3.11 of Červený<sup>29</sup>.

A termination line is constructed within the structure, perpendicularly to the vector joining the ray source to the ray target. Rays propagate from the source and terminate somewhere along this line. The distance along the termination line between the ray intercept and the target is used to select the phase angle at which the next ray is launched. For example, in Fig. 2, a ray launched at angle  $\theta_1$  terminates below the ray target and a second ray at angle  $\theta_2$  terminates above. Linear interpolation uses the measures of distance  $d_1$  and  $d_2$  to select a phase angle in between the angles of the previous two attempts. This is repeated until the ray locates the target point within a particular margin of error.

When the required ray is found, five properties are assigned to the target point:

- (i)  $H_T$ , the total time taken for the ray to reach the target.
- (ii)  $H_P$ , the change in phase due to interaction with physical and non-physical boundaries, as given by theory in Sec. II. B.
- (iii)  $H_B$ , a fraction describing the change in ray energy due to interaction with physical and non-physical boundaries.
- (iv)  $H_D$ , a fraction describing the change in ray energy due to divergence. To compute this value, two outside rays are propagated at  $4'$  to either side of the Fermat ray for a length of time given by  $H_T$ . The final positions of these two rays, along with the final position of the central Fermat ray, are used to define an arc, the length of which is to be called  $l_D$  (see Fig. 3). The change in energy is then given by

$$\frac{\theta d_0}{l_D} \tag{16}$$

with  $\theta$  as the angular spread and  $d_0$  as a short reference distance from the starting position of the ray. This expression would not be applicable if a caustic ray lies anywhere within the outside rays.

- (v)  $H_E$ , the product of  $H_B$  and  $H_D$ , is a fraction describing the total energy change.

This method is used to generate both the artificial signal data and the delay law data, the latter being used to focus the former via the techniques described in Sec. V. The procedure outlined above can also be applied to half-skip and full-skip inspection types<sup>30</sup> by allowing reflection from the backwall, as illustrated in Fig. 4. In these cases, the weld is 'unfolded' and

the reflected space is drawn below the non-reflected space with the backwall acting as a mirror.

Examples of the graphical representation of the variation of these five properties across the weld model are shown in Fig. 5 for an SV wave that converts to a P wave after reflection at the backwall, together with the corresponding ray-tracing diagrams and plots showing coverage for the array. In the figure, a 16-element simulated transducer array is situated such that its ends are at  $(x,z) = (28,58)$  and  $(58,58)$ . The weld parameters used are:  $T=1.0$ ;  $D=2.0$ ;  $\eta=1.0$  and  $\alpha=\arctan(0.4)$ . White sections on the figures (with the exception of 5(c)) indicate areas that are hard to access ultrasonically for reasons of either model geometry or for reasons of beam steering due to material properties.

## V. IMAGING ALGORITHMS

A passive imaging system consists of an array of transducers acting as receivers, to extract information from an area of material in much the same way human sight draws information from the surrounding environment. By contrast, the transducers of an active system act both as receivers and transmitters. One or more of the transducers, acting as a transmitter, emits a pulse, whose reflections are received by the same set of transducers acting as receivers. The imaging algorithms presented here process these received signals to focus the energy in the post-processing domain on a particular point within the test space. The process repeats for a grid of points and the relative amplitudes of the responses are plotted to create an image. An excellent overview of ultrasonic imaging may be found the first chapter of<sup>30</sup>.

The important elements of the forward model are the propagation and the nature of the interaction with defects, which, for the purposes of this paper, comprises only reflectivity. Having been reflected from a series of defects, the wave field function  $W$  at the receiver position  $\zeta_{rx}$  can be written as

$$W(\zeta_{rx}) = P(\zeta_{rx}, \zeta_1)R(\zeta_1)P(\zeta_1, \zeta_{tx})W(\zeta_{tx}) \quad (17)$$

where the operator  $P(\zeta_a, \zeta_b)$  describes the change in wave field properties due to the propagation from  $\zeta_b$  to  $\zeta_a$  and operator  $R(\zeta_1)$  describes the reflectivity of the various image features (defects or the backwall) at position  $\zeta_1$ , the original signal being written as  $W(\zeta_{tx})$ . Here, the wave field function comprises data such as wave energy, divergence, phase and time of flight.

If, as is the case in the half-skip inspection mode, there are two reflections, the wave field function is governed by the expression

$$W(\zeta_{rx}) = P(\zeta_{rx}, \zeta_2)R(\zeta_2)P(\zeta_2, \zeta_1)R(\zeta_1)P(\zeta_1, \zeta_{tx})W(\zeta_{tx}). \quad (18)$$

Two different algorithms are used in this paper. The total focusing method<sup>31</sup> (TFM) processes echoes from all possible send-receive combinations in the phased array, thus extracting the maximum possible amount of information from the specimen. The array is then focused on every image point in turn through sampling the data matrix at a time given by the delay laws, after the acquisition of data, to generate the image. If the signal data are contained in the matrix  $S_{tx,rx}(t)$  and the required time delays for the sending and receiving legs of the ray journey were  $H_{T,tx}$  and  $H_{T,rx}$  respectively, then the production of the image response matrix  $I$  is given by

$$I(x, z) = \left\| \sum_{tx} \sum_{rx} S_{tx,rx} (H_{T,tx} + H_{T,rx}) \right\| \quad (19)$$

where  $tx$  indicates the transmitting element and  $rx$  the receiving element.

The Synthetic Aperture Focusing Technique<sup>31</sup> (SAFT), a variation on TFM, processes only those echoes where the sending and receiving element in the array are the same. The SAFT process compromises completeness of data acquisition for a more rapid computation process; it requires  $n_{\text{elem}}$  summations where  $n_{\text{elem}}$  is the number of elements in the array, whereas TFM requires  $\frac{1}{2}n_{\text{elem}}(n_{\text{elem}}-1)$  summations. The transmit-receive matrices of these algorithms are illustrated in Fig. 6.

## VI. IMAGING WITH THE RAY MODEL

### A. Procedure

The calculations are performed in the frequency domain for the examples in this section. A toneburst modified by a Hanning window is applied to simulate reflected signals, whose function  $B(a)$  in a form discretised according to time, is given by

$$B(a) = \frac{1}{2} \left[ 1 - \cos \left( \frac{2\pi(a-1)}{n_{\text{samples}}} \right) \right] \sin \left( \frac{4\pi(a-1)n_c}{n_{\text{samples}}} \right) \quad \left. \begin{array}{l} 1 \leq a \leq n_{\text{samples}} \\ B(a) = 0 \quad n_{\text{samples}} < a \end{array} \right\} \quad (20)$$

with  $a$  as a dummy variable, where  $n_{\text{samples}}$  is the number of time samples and  $n_c$  is the number of cycles. The function in (20) is zero-padded (i.e.  $n_f \geq n_{\text{samples}}$ ; the number of samples in the frequency domain is greater than or equal to the number of samples in the time domain) and then transformed via the discrete fast Fourier transform. The discretised frequencies used during image compilation due to the transform are given by the expression

$$J_f(b) = f_c \left( \frac{(n_f + 1)(n_c - 2) - 4b}{(n_f + 1)n_c} \right) \quad (21)$$

for  $1 \leq b \leq n_f$  where  $n_f$  is the number of frequency samples and  $f_c$  is the centre frequency. The relative amplitudes associated with the frequencies in (21) are the discretised magnitudes of the Fourier transform:

$$J(b) = \|\mathbb{F}\{B((n_f + 1)(n_c - 2) - 4b + 1)\}\|; 1 \leq b \leq n_f \quad (22)$$

where  $\mathbb{F}\{B\}$  indicates the Fourier transform of the function  $B$ . In the interests of computational efficiency, delay law calculations are performed in two stages: once for the journey towards the defect and once for the journey away from the defect. In this model, uniform and lossless reflectivity at the defect, no change in phase for an SH wave and a change of  $\pi$  for SV and P waves are assumed.

From this point let us assign the superscripts + and - to denote rays travelling towards and away from a defect, and the superscripts s and d to denote signal data and delay law data respectively. Signal data are:

- (i) Shifted in time by a factor  $\Phi_T$ ; the difference in time of flight between the signal data and delay law data.
- (ii) Adjusted in energy by a factor  $\Phi_E$ ; the total predicted drop in energy. To calculate the total drop in energy due to boundary interaction the  $H_B$  terms can be multiplied directly but to calculate the total drop in energy due to ray divergence the  $H_D$  terms must be combined as shown in (23) within the square root.
- (iii) Adjusted in phase by  $\Phi_P$ .

$$\begin{cases} \Phi_T = H_T^{s+} + H_T^{s-} - H_T^{d+} - H_T^{d-} \\ \Phi_E = \frac{1}{H_B^{s+} H_B^{s-}} \sqrt{\frac{1}{(H_D^{s+})^2} + \frac{1}{(H_D^{s-})^2}} \\ \Phi_P = H_P^{s+} + H_P^{s-} \end{cases} \quad (23)$$

Variations on these factors are discussed in Sec. VI.B. The factors are fed into the expression

$$I(x, z) = \left\| \sum_{b=1}^{n_f} \sum_{tx} \sum_{rx} J(b) \sqrt{\Phi_E} \exp(2\pi i J_f(b) \Phi_T + i \Phi_P) \right\| \quad (24)$$

to yield the amplitude of the image intensity  $I$  at a particular point, operating over the full range of frequencies according to (22).

## B. Results

A simulated array containing 32 elements is positioned such that the centre of the nearest element is 31mm from the weld centreline. The weld, whose geometry is illustrated in Fig. 7, is symmetrical and the weldment is of the materials used previously in Sec. IV. Directivity associated with individual elements has been ignored in this paper.

In Fig. 7, the results of the imaging of a crack-like defect are shown. The crack, 5.4mm in length, has been modelled as a series of 32 point defects according to the Huygens principle. The simulated inspection is carried out using SH waves that reflect from the weld backwall without converting to a different mode, before taking the same path back to the receiving element. Both the SAFT and the TFM algorithms are demonstrated with an interrogating frequency of 1.6MHz.

The defect is more accurately located when the delay laws that correspond to the anisotropic weld ('matching' delay laws) have been used in Fig. 7(c) and Fig. 7(e), where it can be seen that the energy has focused on both tips of the crack. If inhomogeneity and anisotropy of the weld were to be ignored (by using 'isotropic' delay laws), then the peaks of the image response in Fig. 7(b) and Fig. 7(d) do not align properly with either tip of the crack and there is a risk of defect mislocation and potential missizing. In this example, using the appropriate delay laws also has the advantage of producing a sharper focusing of energy about the defect tips. Generally, the SAFT images show a tighter concentration of energy about the tips of the defect but TFM is superior in suppression of spurious image features.

### **C. Adjusting for amplitude response**

It can be seen from (23) that the possibility exists to adjust the generated image to compensate for the different amounts of ultrasonic energy reaching different portions of the weld. In this section, it is suggested that image features that are weak can be enhanced and brought into parity with stronger features. It is also suggested that features lying in an area partially blind to the array can be similarly enhanced. Here the procedure is briefly demonstrated.

In Fig. 8, using SH waves, TFM images of a weld with six point defects at equally spaced intervals between (-20,10)mm to (30,10)mm. The image responses from the three defects on the left are predicted to be weaker due to the lower amounts of energy reaching those areas (Fig. 8(a)) and poorer array coverage (Fig. 8(b)). The unadjusted TFM image is shown in Fig. 8(c) with an attached cross-section at  $z=10$ mm. If this image is adjusted to compensate for the different predicted amounts of energy reaching each image point, then this modified energy factor  $\Phi'_E$  would be used instead, defined in terms of the original energy factor

$$\Phi'_E = \frac{H_B^{d+} H_B^{d-}}{\sqrt{\frac{1}{(H_D^{d+})^2} + \frac{1}{(H_D^{d-})^2}}} \cdot \Phi_E \quad (25)$$

in (24) and would obtain Fig. 8(d), where it can be seen that the response of the defect farthest to the left has been augmented to match those of the three defects on the right.

It is similarly possible to further adjust the image according to array coverage using the expression

$$\left\{ \begin{array}{ll} \Phi'_E = \frac{n_{\text{elem}}}{n_a} \cdot \Phi_E & n_{\text{elem}} > 0 \\ \Phi'_E = 0 & n_{\text{elem}} = 0 \end{array} \right. \quad (26)$$

to modify the energy factor to compensate for the different number of elements  $n_a$  able to access each image point, resulting in Fig. 8(e). Here the response of the defect that lies within the weld has been augmented but not to the level of those to the right because of the difference in energy reaching the defects. However, applying both (25) and (26) (see Fig. 8(f)) does bring all defect responses into parity. The peak values of the defects in Fig. 8(c) to Fig. 8(f) are shown in Table IV.

In theory, this principle could be extended to adjust images according to the predicted change in phase. Though it is not demonstrated here, the phase factor would then become

$$\Phi'_P = \Phi_P - H_P^{d+} - H_P^{d-} . \quad (27)$$

## VII. IMAGING WITH FE SIMULATIONS

The aim of this section is to demonstrate the imaging of a simple defect using the synthetically focused imaging algorithms of Sec. V to process data gathered in finite element simulations via the application of delay laws whose computation was described in Sec. IV.

### **A. Procedure**

A 2D finite element model was built using the software package ABAQUS/Explicit as the inspection environment, using dimensions equivalent to those shown in the previous section. A FORTRAN routine controlled the specific mesh generation due to the spatially varying properties. The model used here is composed of a grid of quadrilateral and triangular plane strain elements, illustrated in Fig. 9(a). All elements are square except for those within the vicinity of the weld, where triangular and rectangular elements, whose ratio of height to width is 2.5, are found (see Fig. 9(b)). The weld model is surrounded on all four sides by a layer of an absorbing material 6.25mm in thickness to eliminate unwanted reflections and to improve the quality of the resulting images. This has been implemented through the use of an absorbing parameter whose value is governed by a cubic expression in terms of the distance from the propagating region, following the guidelines as given by Drozd et al.<sup>32</sup>

In order to satisfy the requirements of the Nyquist sampling criterion, the minimum wavelength is chosen to be double the elemental spacing of the receivers, and since this spacing is 8 elements, then the maximum frequency is  $f_{\max}=c/(16d)$  where  $d$  is the element pitch. Thus, for a longitudinal interrogating signal, the frequency is in the order of 3MHz. Excitation was provided by means of the forced displacement of a single node within the weld model. This took the form of a toneburst of two cycles modulated by a Hanning window, with a polarisation vector oriented such that the strongest part of the wave would reach the central elements of the transducer array. Ray-tracing models were used to inform the choice of this vector.

For each image of a point defect, the simulation was run once. Complete recorded time histories of each of the receiving nodes were extracted where the array acts solely as a receiver. Since the model only deals with waves returning to the array, there is no dependency on  $S_{ix}(t)$ . The image matrix  $I(x,z)$  is therefore compiled according to the equation

$$I(x, z) = \left\| \sum_{rx} S_{ix,rx} (H_{T,rx}) \right\|. \quad (28)$$

## B. Results

Examples of the resulting images are shown in Fig. 10. The images show the response from a single point defect located at (-13,27)mm using the SAFT algorithm to focus the signal data from the FE weld model. It is seen that when isotropic delay laws are used, the energy has not focused in the correct place, the image peak being 5.3mm (more than 10 wavelengths distant) from the known location of the defect. If the correct matching delay laws are used, then the image response overlaps with the defect. Thus the technique reported here has the potential to overcome material inhomogeneity in order to correct images with the aim of locating point reflectors.

## VIII. CONCLUSIONS AND PERSPECTIVES

Using a previously developed weld model as the inspection environment, this paper has presented an overview of ray-tracing principles through strongly inhomogeneous and complex anisotropic materials. These techniques allow the computation of delay laws applicable to a simulated transducer array. It has been shown that it is possible to predict, from fundamental ray propagation theory, the Fermat path of a ray to reach a particular point, the ray energy, and the coverage of a weld region for a given array. Simulated images of a

simple crack-like defect were produced from broadband signals using the computed delay laws. Finally, these laws were used to locate point defects in an FE model. It has been demonstrated that mislocation (which itself may lead to missizing) may occur if the inhomogeneity and the anisotropy are ignored. For image correction, the importance of using delay laws corresponding to the correct material and using laws that represent the inhomogeneous properties of the weld has been emphasised.

Although the work in this paper has been performed in the specific application of the improved inspection of austenitic steel welds, these imaging methods and image correction are of general applicability to other disciplines, such as seismology in oil exploration, and other materials, such as composites, as long as a model of the spatial variation of material properties is provided. Once such a model is provided, these improvements would be ready for implementation in applications involving ray-tracing techniques.

The ray-tracing model has limitations that are to be addressed in future work. The model currently ignores directivity of either the array element or the defects. It is thought that elemental directivity such as that used by Hunter et al.<sup>33</sup> can be implemented and that scattering matrices<sup>34</sup> can be incorporated into the model to produce more realistic behaviour of energy reflection. The limitations of the FE are due in particular to the coarser nature of discretisation when compared with the ray-tracing model. There is certainly continuing scope for greater understanding of the FE mesh behaviour to inform techniques that would improve imaging resolution. Work may also extend to the production of sharper images dealing with signals reflected from the backwall.

## **ACKNOWLEDGEMENTS**

This research was undertaken as part of the research program of the UK Research Centre in NDE (RCNDE) with support from the EPSRC.

## References

- <sup>1</sup> R. Long, J. Russell, P. Cawley, and N. Habgood, "Ultrasonic phased array inspection of flaws on weld fusion faces using full matrix capture", *Rev. Qnt. NDE, AIP Conf. Proc.* **1096** 848-855 (2008).
- <sup>2</sup> A. Apfel, J. Moysan, G. Corneloup, T. Fouquet, and B. Chassignole, "Coupling an ultrasonic propagation code with a model of the heterogeneity of multipass welds to simulate ultrasonic testing", *Ultrasonics* **43(6)**, 447-456 (2004).
- <sup>3</sup> C. Gueudre, L. Le Marrec, J. Moysan, and B. Chassignole, "Direct model optimisation for data inversion. Application to ultrasonic characterisation of heterogeneous welds", *NDT&E Int.* **42(1)**, 47-55 (2008).
- <sup>4</sup> P. Bovik and A. Bostrom, "Model of ultrasonic non-destructive testing for internal and sub-surface cracks", *J. Accout. Soc. Am.* **102**, 2723-2733 (1997).
- <sup>5</sup> J. Ford, and R. J. Hudgell, "A final report on the performance achieved by non-destructive testing of defective butt welds in 55mm thick type 316 stainless steel", *Pub. NDT Dev. & Appl. Dept., Risley Nuclear Power Development Laboratories* (1987).
- <sup>6</sup> A. H. Harker, J. A. Ogilvy, and J. A. G. Temple, "Modeling ultrasonic inspection of austenitic welds", *J. NDE* **9(2/3)**, 155-165 (1990).
- <sup>7</sup> Y. Cui, and C. D. Lundin, "Austenite-preferential corrosion attack in 316 austenitic stainless steel weld metals", *Mat. & Design* **28(1)**, 324-328 (2007).
- <sup>8</sup> W. E. Gardner, "Improving the effectiveness and reliability of non-destructive testing", *Pub. Paragon Presss* (1992).
- <sup>9</sup> X. Edelmann, "Application of ultrasonic testing techniques on austenitic welds for fabrication and in-service inspection", *NDT Int.* **1981**, 125-133 (1981).
- <sup>10</sup> X. Edelmann, "Addressing the problem of austenitics", *Nucl. Eng. Int.* **1989**, 32-33 (1989).

- <sup>11</sup> R. J. Hudgell, G. M. Worrall, J. Ford, and B. S. Gray, "Ultrasonic characteristics and inspection of austenitic welds", *Int. J. Press. Vessels & Piping* **39**, 247-263 (1989).
- <sup>12</sup> F. I. Federov, *Theory of elastic waves in crystals*, (Plenum, New York) (1968).
- <sup>13</sup> D. Kupperman, and K. Reiman "Ultrasonic wave propagation and anisotropy in austenitic stainless steel weld metal", *IEEE Trans. Son. Ultrason.* **SU27**, 7-15 (1980).
- <sup>14</sup> M. Silk, *Ultrasonic Techniques for Inspecting Austenitic Welds, Research Techniques in NDT*, Vol IV, chpt. 11, pp 393-449 (Academic Press, London) (1980).
- <sup>15</sup> Chassignole, B., Diaz, J., Duwig, V., Fouquet, T., and Schumm A. (2006) "Structural noise in modelisation," *Proc. ECNDT 2006 – Fr.1.4.4* 1-13
- <sup>16</sup> S. Halkjær, M. P. Sørensen, and W. D. Kristensen, "The propagation of ultrasound in an austenitic weld", *Ultrasonics* **38**, 256-261 (2000).
- <sup>17</sup> R. Halmshaw, *Non-destructive Testing*, Chpt. 11, pp 393-449 (Arnold) (1991).
- <sup>18</sup> J. A. Ogilvy, "Ultrasonic ray-tracing in austenitic steel using RAYTRAIM: Ray-tracing in Anisotropic Inhomogeneous Media", *NDT Int.* **18(2)**, 67-77 (1984).
- <sup>19</sup> A. H. Harker, *Elastic waves in solids with applications to nondestructive testing of pipelines*, (Adam Hilger, Bristol and Philadelphia) (1988).
- <sup>20</sup> S. Russel, "Report on waves", *Br. Assoc. Rep.* 369 (1844).
- <sup>21</sup> Lord Rayleigh, "On the velocity of light", *Nature* **XXIV**, 382 (1881).
- <sup>22</sup> K. Goebbels, *Materials Characterization for Process Control and Product Conformity*, (CRC Press, Boca Raton FL) (1994).
- <sup>23</sup> S. I. Rokhlin, K. Bolland, L. Adler, "Reflection and refraction of elastic waves on a plane interface between two generally anisotropic media", *J. Acoust. Soc. Am.* **79**, 906-918 (1986).
- <sup>24</sup> P. Lancelleur, H. Ribeiro, and J.-F. De Belleval, "The use of inhomogeneous waves in the reflection-transmission problem at a plane interface between two anisotropic media", *J. Acoust. Soc. Am.* **93**, 1882-1892 (1993).

- <sup>25</sup> R. A. Roberts, "Ultrasonic beam transmission at the interface between an isotropic and a transversely isotropic solid half space", *Ultrasonics* **26**, 139-147 (1988).
- <sup>26</sup> Anon, "ABAQUS theory manual ver. 6.5", (Hibbit, Karlsson & Sorensen, Inc., Pawtucket RI) (2008).
- <sup>27</sup> G. D. Connolly, M. J. S. Lowe, S. I. Rokhlin, and J. A. G. Temple, "Application of Fermat's principle to the improved inspection of austenitic steel welds", *Proc. R. Soc. A* **465**: 3401-3423 (2009).
- <sup>28</sup> M. Epstein, and J. Sniatycki, "Fermat's principle in elastodynamics", *J. Elasticity* **27**, 45-56 (1992).
- <sup>29</sup> V. Červený, *Seismic ray theory*, (Cambridge University Press, Cambridge UK) (2001).
- <sup>30</sup> Anon., *Introduction to Phased Array Ultrasonic Technology Applications*, (R/D Tech Inc., Québec, Canada) (2004).
- <sup>31</sup> R. Y. Chiao, L. J. Thomas, "Analytical evaluation of sampled aperture ultrasonic imaging techniques for NDE", *IEEE Trans. Ultrason., Ferroelectr. Freq. Control* **41(4)**, 484-493 (1994).
- <sup>32</sup> M. B. Drozdz, E. Skelton, R. V. Craster, M. J. S. Lowe, "Modeling bulk and guided waves in unbounded elastic media using absorbing layers in commercial finite element packages", *Rev. Qnt. NDE, AIP Conf. Proc.* **894** 87-94 (2007).
- <sup>33</sup> A. J. Hunter, B. W. Drinkwater, P. D. Wilcox, "The Wavenumber Algorithm for Full-Matrix Imaging Using an Ultrasonic Array", *IEEE Trans. Ultrason. Ferroelectr. Freq. Control* **55(11)**, 2450-2462 (2008).
- <sup>34</sup> J. Zhang, B. W. Drinkwater, and P. D. Wilcox, "The Use of Scattering Matrix to Model Multi-Modal Array Inspection with the TFM", *Rev. Qnt. NDE, AIP Conf. Proc.* **1096** 888-895 (2009).

## LIST OF FIGURES

FIG. 1. The physical significance of the weld parameters for the weld model<sup>17</sup>.

FIG. 2. Trial-and-error method applied to the problem of joining the ray source to the ray target via a Fermat path.

FIG. 3. Computation of divergence of a ray joining the source to the target.

FIG. 4. The procedure of Fig. 3 applied to an inspection procedure involving backwall reflection, illustrated in (a) unfolded space and (b) folded space.

FIG. 5. The following properties of an SV ray that converts to a P ray upon reflection at the backwall, source at  $(x,z) = (42,58)$ mm, are illustrated as a function of ray termination position: (a) original ray-tracing diagram, (b) time delay or time of flight in seconds, (c) overall coverage fraction for all sixteen elements in the transducer array, (d) logarithmic plot of the fraction of energy remaining due to ray divergence, (e) logarithmic plot of the fraction of energy remaining due to boundary interaction and (f) change in phase due to boundary interaction. Where relevant, quantities are given by the shade indicated in the scale to the right of the diagram; for (b), (d), (e) and (f), white areas indicate inaccessibility.

FIG. 6. The transmit-receive matrices for (a) SAFT and (b) TFM.

FIG. 7. Imaging of a crack-like defect whose ends are at  $(-16,45)$ mm and  $(-18,50)$ mm, using full-skip SH wave inspection: (a) weld geometry and the crack location; (b) SAFT image

using isotropic delay laws; (c) SAFT image using matching delay laws; (d) TFM image using isotropic delay laws and (e) TFM image using matching delay laws.

FIG. 8. Imaging of six point defects spaced at 10mm intervals from (-20,10)mm to (30,10)mm, showing, as a function of image point position: (a) logarithmic plot of the total fraction of energy remaining and (b) overall coverage fraction for all the elements in the transducer array. Also shown are TFM images of the defects with: (c) no adjustment; (d) adjustment for energy fraction only; (e) adjustment for array coverage only and (f) adjustment for both energy fraction and array coverage.

FIG. 9. (a) Structure of the FE model used for simulations. Figures refer to the number of elements along the dimension indicated. (b) Detail of the weld boundary region.

FIG. 10. Imaging of FE simulation results for a point defect at (-13,27)mm, compiled using (a) matching delay laws and (b) isotropic delay laws.

TABLE I: Summarised properties of evanescent waves.

	<b>Propagating waves</b>	<b>Evanescant waves</b>
Phase vector	Real	Vertical part has imaginary component
Group vector	Real	Meaningless; energy does not propagate
Polarisation vector	Real	Vertical part has imaginary component
Energy flux density vector	Component normal to interface is real and nonzero	Purely imaginary

TABLE II: Material properties for the transversely isotropic steel<sup>25</sup>. Voigt notation applies

<b>Material parameter</b>	<b>Value</b>
$C_{11}$	$249 \times 10^9 \text{ Nm}^{-2}$
$C_{12}$	$124 \times 10^9 \text{ Nm}^{-2}$
$C_{13}$	$133 \times 10^9 \text{ Nm}^{-2}$
$C_{33}$	$205 \times 10^9 \text{ Nm}^{-2}$
$C_{44}$	$125 \times 10^9 \text{ Nm}^{-2}$
$C_{66}$	$62.5 \times 10^9 \text{ Nm}^{-2}$
density $\rho$	$7.85 \times 10^3 \text{ kgm}^{-3}$

TABLE III: Material properties for the isotropic mild steel. Voigt notation applies

<b>Material parameter</b>	<b>Value</b>
$C_{11}$	$283 \times 10^9 \text{ Nm}^{-2}$
$C_{12}$	$121 \times 10^9 \text{ Nm}^{-2}$
$C_{13}$	$121 \times 10^9 \text{ Nm}^{-2}$
$C_{33}$	$283 \times 10^9 \text{ Nm}^{-2}$
$C_{44}$	$80.7 \times 10^9 \text{ Nm}^{-2}$
$C_{66}$	$80.7 \times 10^9 \text{ Nm}^{-2}$
density $\rho$	$7.85 \times 10^3 \text{ kgm}^{-3}$

TABLE IV: Peak image response of the six defects in Fig. 8, shown as a percentage of that of the defect on the right.

<b>defect position</b>	<b>(-20,10)</b>	<b>(-10,10)</b>	<b>(0,10)</b>	<b>(10,10)</b>	<b>(20,10)</b>	<b>(30,10)</b>
unadjusted	0.6346	0.2412	0.0255	0.9474	0.9781	1.0000
adjusted for energy fraction	1.0701	0.4773	0.0686	1.0215	1.0119	1.0000
adjusted for array coverage	0.6345	0.4669	0.3783	0.9474	0.9781	1.0000
adjusted for both energy fraction and array coverage	1.0700	0.9237	1.0226	1.0215	1.0119	1.0000

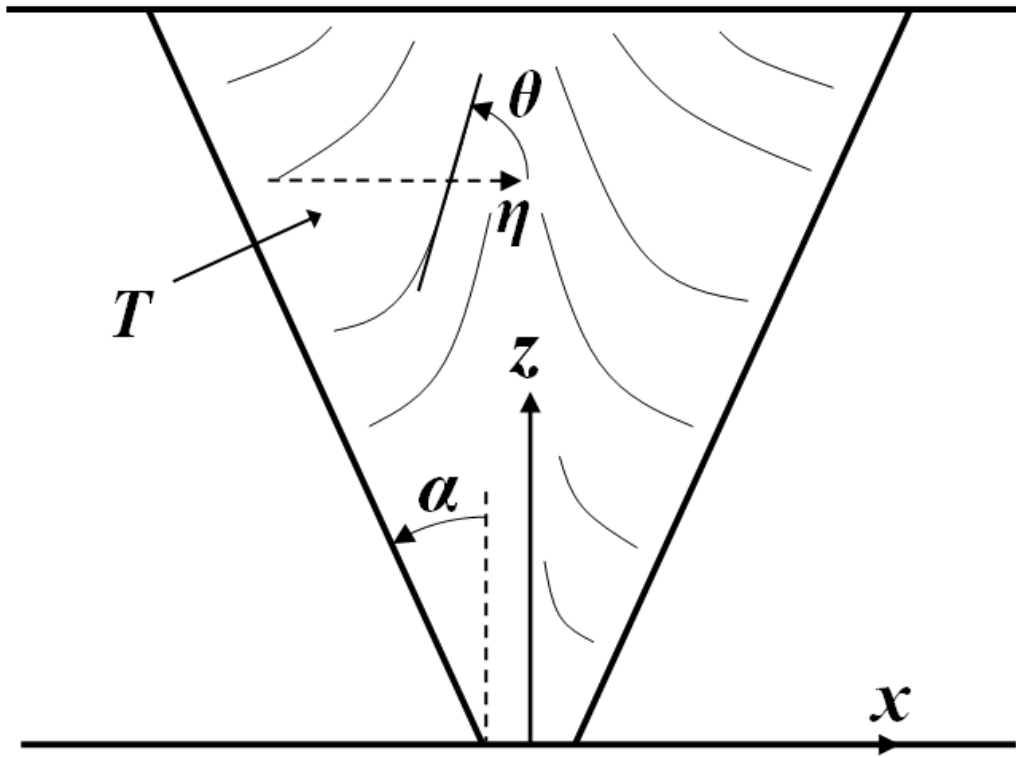


FIG. 1. The physical significance of the weld parameters for the weld model<sup>17</sup>.

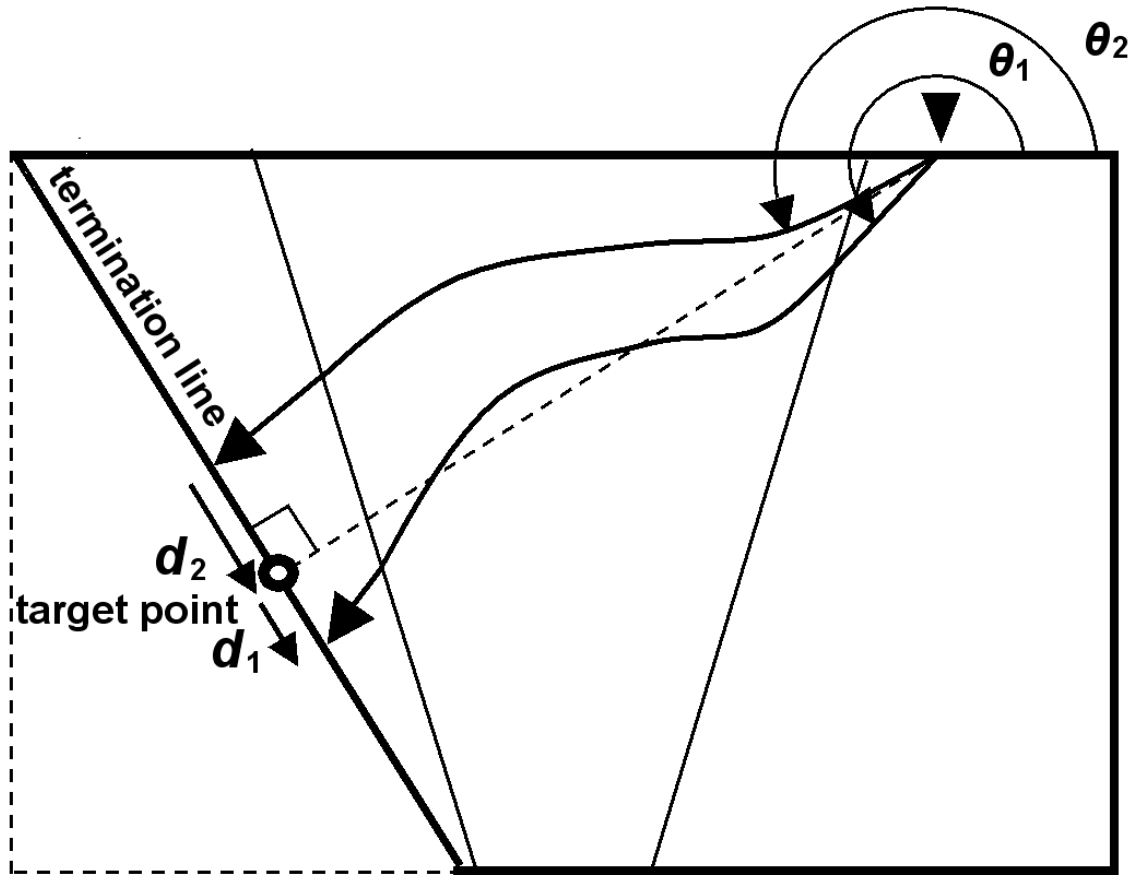


FIG. 2. Trial-and-error method applied to the problem of joining the ray source to the ray target via a Fermat path.

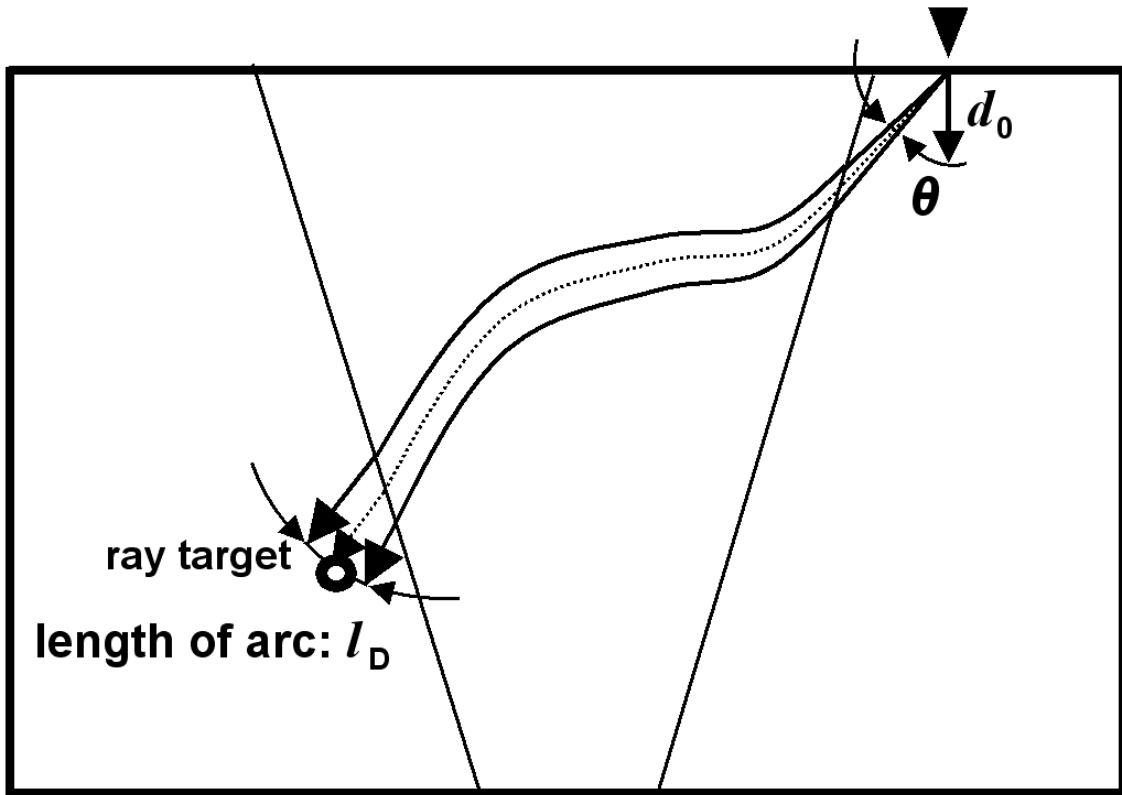


FIG. 3. Computation of divergence of a ray joining the source to the target, showing reference distance  $d_0$ , angular spread  $\theta$  and arc length  $l_D$  as applied to three rays that have propagated for the same length of time.

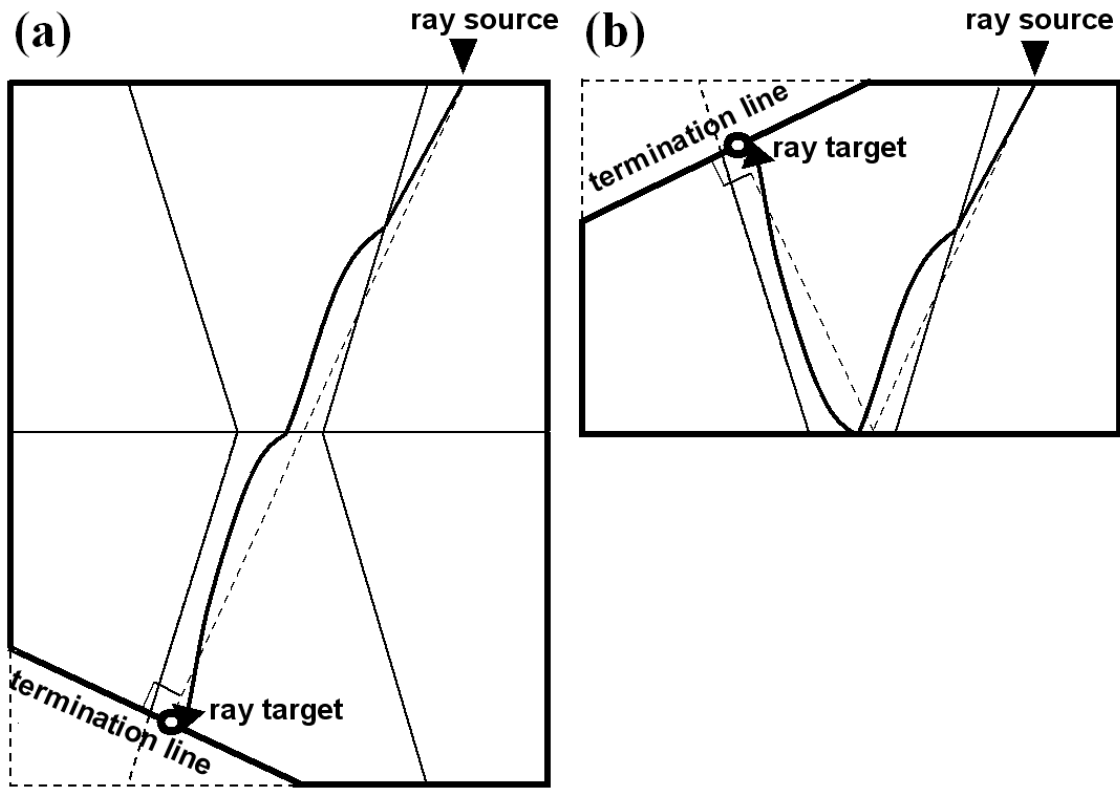


FIG. 4. The procedure of Fig. 3 applied to an inspection procedure involving backwall reflection illustrated in (a) unfolded space and (b) folded space.

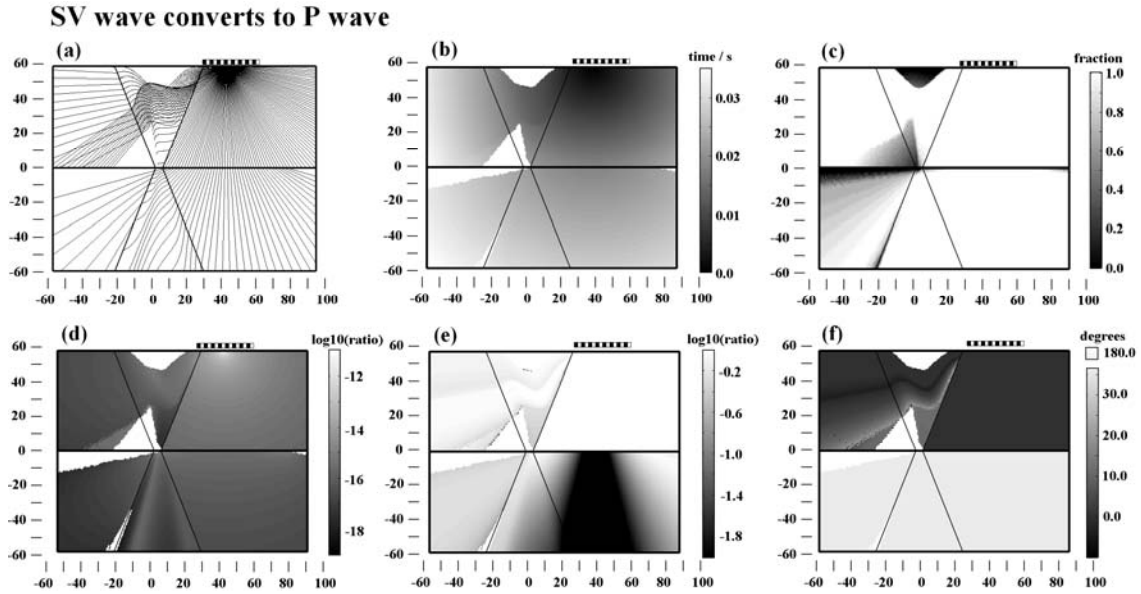


FIG. 5. The following properties of a vertically polarised transverse ray that converts to a longitudinal ray upon reflection at the backwall and whose source is located at  $(x,z) = (42,58)$ mm, the sixth element of the array from the left, are illustrated as a function of ray termination position: (a) original ray-tracing diagram, (b) time delay or time of flight in seconds, (c) overall coverage fraction for all sixteen elements in the transducer array, (d) logarithmic plot of the fraction of energy remaining due to ray divergence, (e) logarithmic plot of the fraction of energy remaining due to boundary interaction and (f) change in phase due to boundary interaction. Where relevant, quantities are given by the shade indicated in the scale to the right of the diagram; for (b), (d), (e) and (f), white areas indicate inaccessible areas.

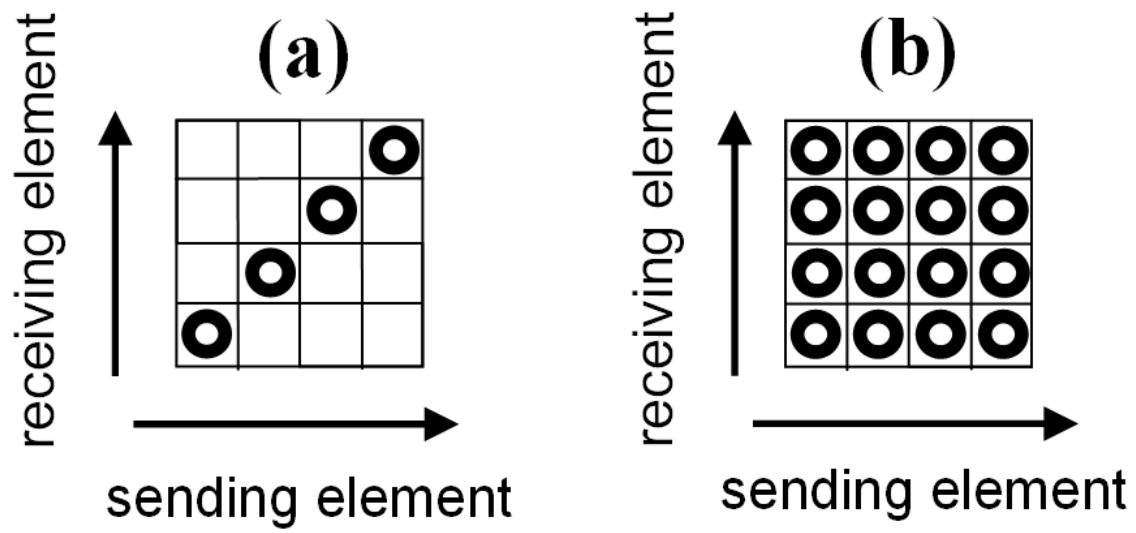


FIG. 6. The transmit-receive matrices for (a) SAFT and (b) TFM.

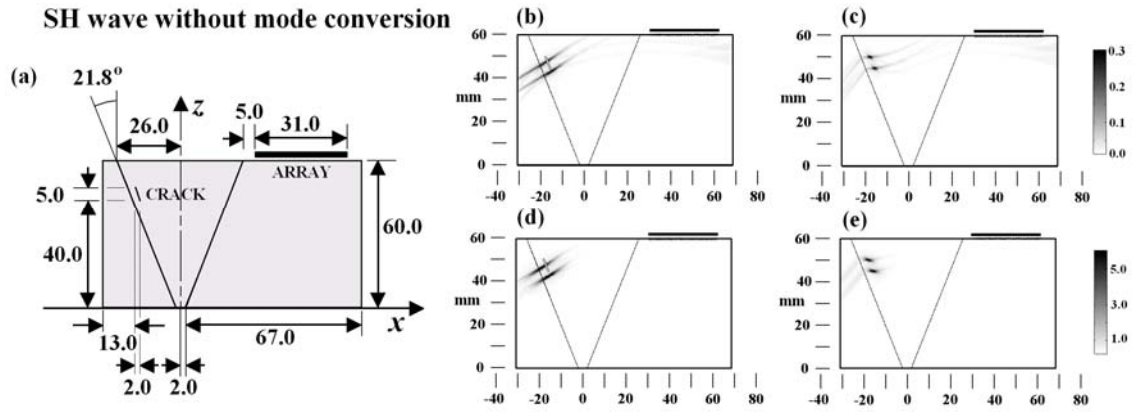


FIG. 7. Imaging of a crack-like defect whose ends are at (-16,45)mm and (-18,50)mm, using full-skip SH wave inspection, illustrating: (a) weld geometry and the crack location; (b) SAFT image using isotropic delay laws; (c) SAFT image using matching delay laws; (d) TFM image using isotropic delay laws and (e) TFM image using matching delay laws.

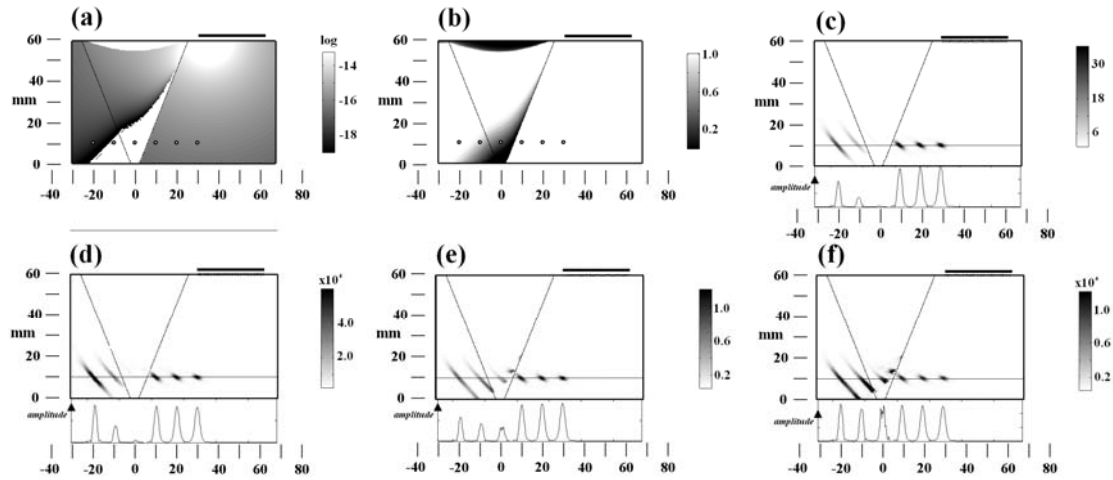


FIG. 8. Imaging of six point defects spaced at 10mm intervals from (-20,10)mm to (30,10)mm, showing, as a function of image point position: (a) logarithmic plot of the total fraction of energy remaining and (b) overall coverage fraction for all the elements in the transducer array. Also shown are the TFM images of the defects with varying levels of adjustment: (a) no adjustment; (b) adjustment for energy fraction only; (c) adjustment for array coverage only and (d) adjustment for both energy fraction and array coverage.

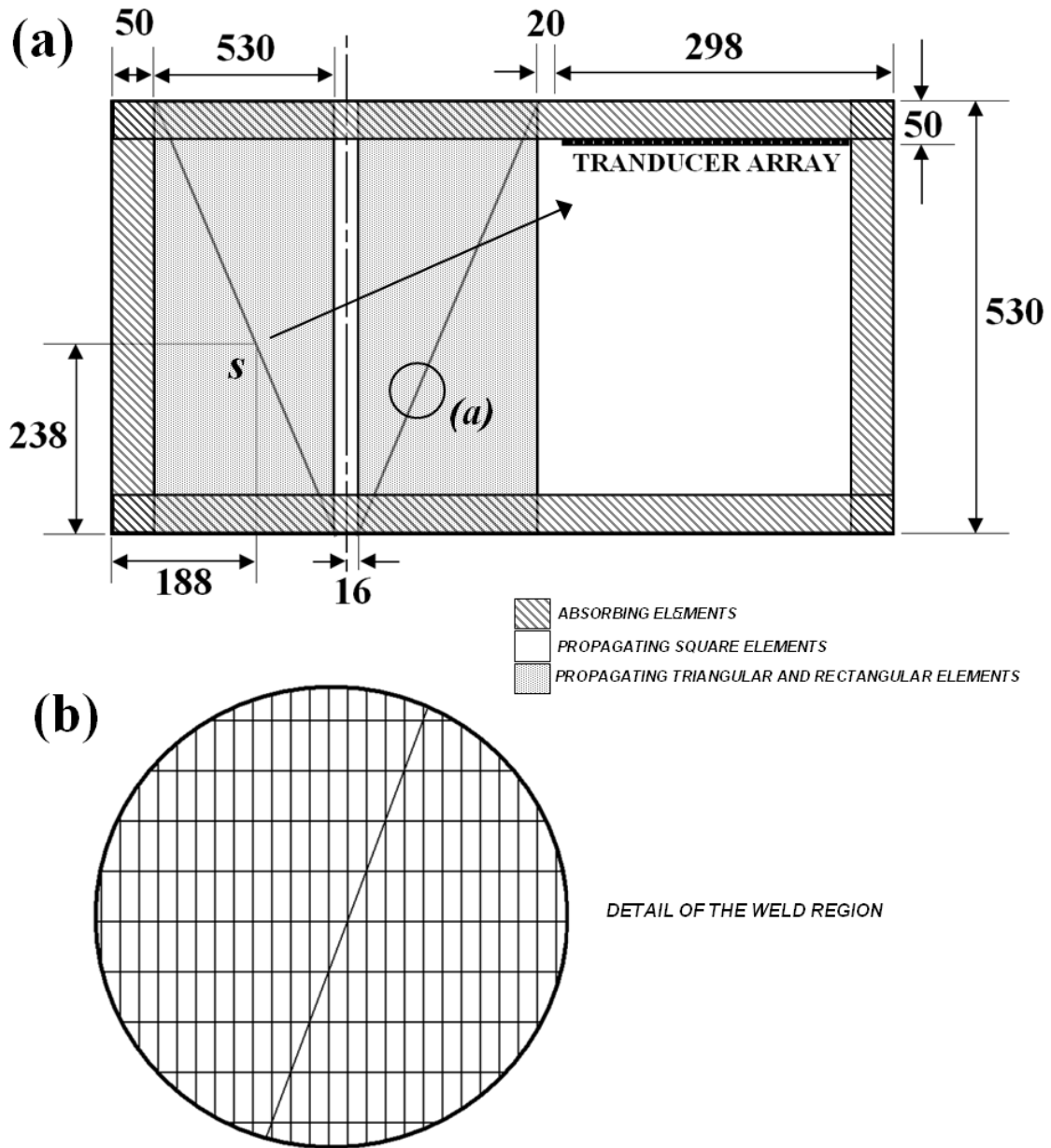


FIG. 9. (a) Structure of the FE model used for simulations. Figures refer to the number of elements along the dimension indicated. White areas are composed entirely of square elements. Elements falling within the striped areas are absorbing. Grey areas are composed of rectangular and triangular elements, as shown in (b).

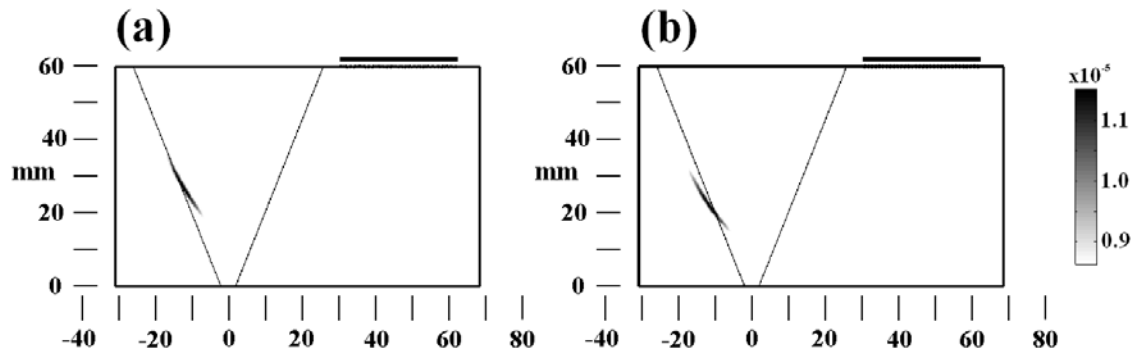


FIG. 10. Imaging of finite element simulation results for a point defect at (-13,27)mm. In (a), matching delay laws are used whereas in (b), isotropic delay laws are used to compile the image.